Journal of Alloys and Compounds 509 (2011) 5420–5425

Contents lists available at ScienceDirect

Journal of Alloys and Compounds

journal homepage: www.elsevier.com/locate/jallcom

Magnetic properties of mechanochemically synthesized γ-Fe_2O_3 nanoparticles

Takuya Tsuzuki[a,c,*], Franziska Schäffel[b,d], Michihito Muroi[c], Paul G. McCormick[b,c]

[a] Institute for Technology Research and Innovation, Deakin University, Geelong, Victoria 3217, Australia
[b] Research Center for Advanced Mineral and Materials Processing, The University of Western Australia, Crawley, Western Australia 6009, Australia
[c] Antaria Limited, Bentley, Western Australia 6102, Australia
[d] Department of Materials, University of Oxford, Oxford OX1 3PH, United Kingdom

ARTICLE INFO

Article history:
Received 18 November 2010
Received in revised form 10 February 2011
Accepted 15 February 2011
Available online 22 February 2011

Keywords:
Nanostructured materials
Oxide materials
Mechanochemical processing
Magnetic property

ABSTRACT

The synthesis of mono-dispersed γ-Fe_2O_3 nanoparticles by mechanochemical processing was demonstrated for the first time, via the solid-state exchange reaction $Fe_2(SO_4)_3 + 3Na_2CO_3 \rightarrow Fe_2(CO_3)_3 + 3Na_2SO_4 \rightarrow Fe_2O_3 + 3Na_2SO_4 + 3CO_2(g)$ and subsequent heat treatment at 673 K. The nanoparticles had a volume-weighted mean diameter of 6 nm and a narrow size distribution with the standard deviation of 3 nm. The particles showed a superparamagnetic nature with the superparamagnetic blocking temperature of 56.6 K. The anisotropy constant was 6.0×10^6 erg/cm^3, two orders of magnitude larger than the magnetocrystalline anisotropy constant of bulk γ-Fe_2O_3. The detailed analysis of the magnetic properties indicated that the γ-Fe_2O_3 nanoparticles had a core–shell structure, consisting of a ferrimagnetic core of ~4 nm in diameter having a collinear spin configuration and a magnetically disordered shell of ~1.2 nm in thickness.

1. Introduction

When magnetic Fe_2O_3 nanoparticles become smaller than the size of magnetic single-domain, they exhibit unique properties such as superparamagnetism, quantum tunnelling of the magnetization and large coercivities [1]. As such, magnetic Fe_2O_3 nanoparticles find potential applications in many areas including high density magnetic information storage devices [2], ferro-fluid [3], magnetic resonance imaging agents [4], hyperthermic treatment of tumours [5], controlled drug delivery [6], bioseparation [7], and transparent magnetic composites [8]. Fe_2O_3 nanoparticles are also of particular importance in the applications as catalysts [9], sensors [10] and photovoltaics [11]. Among many polymorphs of Fe_2O_3, γ-Fe_2O_3 (maghemite) and Fe_3O_4 (magnetite) have strong magnetic properties. Although both γ-Fe_2O_3 and Fe_3O_4 are a spinel ferrite having similar cubit crystal structures, γ-Fe_2O_3 is chemically more stable and thus the most widely used material for magnetic recording applications [12].

In the past, a variety of methods have been developed for the synthesis of iron oxide ultrafine powders, including sputtering, vapour decomposition, hydrothermal, solvothermal, sol–gel, γ-irradiation and electrochemical processes [9,13–15]. In recent years, mechanochemical processing has been demonstrated as a versatile process for the synthesis of nanoparticles [16,17]. This synthesis technique is of technological interest since the process is relatively simple with only a few operation parameters and is suitable for large quantity production at commercial scale. Of significance is the fact that this technique allows the formation of separated nanoparticles embedded in a solid salt matrix, leading to ultrafine particles with a very low degree of agglomeration [18]. Previously, the mechanochemical synthesis of hematite ultrafine powders was attempted via the reaction $2FeCl_3 + 3Ca(OH)_2 \rightarrow Fe_2O_3 + 3CaCl_2 + 3H_2O$ [19,20]. However, the resulting particles were hard aggregates or polycrystallites of ~100 nm in diameter having grain sizes of 20–30 nm. In this study, the production of Fe_2O_3 nanoparticles by mechanochemical processing via a new reaction route,

$$Fe_2(SO_4)_3 + 3Na_2CO_3 \rightarrow Fe_2(CO_3)_3 + 3Na_2SO_4 \quad (1)$$

$$Fe_2(CO_3)_3 \rightarrow Fe_2O_3 + 3CO_2 \quad (2)$$

was investigated. The reaction (1) has a negative Gibbs free energy change of – 362 kJ/mole at 100 °C and hence, this reaction is potentially mechanically activated in a ball mill [21].

2. Experimental procedure

The starting materials used were $Fe_2(SO_4)_3 \cdot 9H_2O$ (Ajax Finechem, >99.88%), Na_2CO_3 (Fluka, >99%) and NaCl (Ajax, >99%). $Fe_2(SO_4)_3 \cdot 9H_2O$ was dehydrated in air at 573 K for 2 h. X-ray diffraction (XRD) measurements of the dried $Fe_2(SO_4)_3 \cdot 9H_2O$ powder showed that the dehydrated powder consisted of two polymorphs of $Fe_2(SO_4)_3$ corresponding to ICDD JCPDS #73-0148 and #42-0225 but hydrated

* Corresponding author at: Institute for Technology Research and Innovation, Deakin University, Geelong, Victoria 3217, Australia. Tel.: +61 3 5227 3205; fax: +61 3 5227 2847.
E-mail address: takuya@deakin.edu.au (T. Tsuzuki).

0925-8388/$ – see front matter © 2011 Elsevier B.V. All rights reserved.
doi:10.1016/j.jallcom.2011.02.073

phases were not detected. The weight loss during drying was 28.6 wt%, identical to the theoretical value expected for the complete dehydration reaction of $Fe_2(SO_4)_3{\cdot}9H_2O$.

The mixture of starting reactants $Fe_2(SO_4)_3$, Na_2CO_3 and NaCl in a molar ratio of 1:3:4.3, was milled with a shaker-type mill (Spex 8000 mixer mill). The NaCl diluent phase was added to decrease the volume fraction of Fe_2O_3 in the heat-treated powder down to 10% to avoid particle agglomeration [16]. The starting powder mixture was sealed in air in a hardened steel vial along with 6 hardened steel balls of 12.7 mm in diameter. The ball to powder mass ratio was 10:1. Milling was performed up to 4 h with the shaking action of 2500 RPM. The as-milled powders were then subjected to isothermal heat treatment for 1 h in air above the decomposition temperature of $Fe_2(CO_3)_3$ that was determined by simultaneous differential thermal analysis and thermogravimetric analysis (TG/DTA) of the as-milled unheated powders. Following the heat treatment, the powder samples were washed several times with de-ionised water using an ultrasonic bath and a centrifuge in order to remove NaCl and the reaction by-product Na_2SO_4.

X-ray diffraction (XRD) measurements were made using a Siemens D5000 X-ray diffractometer with Cu Kα radiation. TG/DTA of the as-milled unheated powders were carried out using a Waters SDT-2360 thermal analysis system, in an alumina crucible at a heating rate of 20 K/min under a constant air flow of 2 cm^3/min. The microstructure of the particles was studied using a Philips 430 transmission electron microscope (TEM). The TEM specimen was prepared by dispersing the washed powder in methanol using an ultrasonic bath followed by drying a drop of solution on a copper grid coated with holey carbon film.

The particle-size distribution of the powders was measured by photo correlation spectroscopy (PCS) using a Nicomp ZLS 380 instrument. The optical properties of nanoparticle suspensions were characterised using a Varian Cary 300 Bio UV–vis spectrophotometer equipped with a Labsphere DL integrating sphere, using a quartz cuvette having an optical path length of 10 mm. Prior to the PCS and UV–vis spectroscopy measurements, a 0.005 wt% particle suspension in diluted HCl aqueous solution (pH 3) was subjected to ultrasonication using an ultrasonic probe for 15 min to ensure good particle dispersion.

The specific surface area of dried powders was measured by Brunauer–Emmett–Teller (BET) 5-points N_2-gas absorption method at 77 K using a Micromeritics Tristar 3000. Magnetic measurements were carried out using a Quantum Design MPMS superconducting quantum interference device (SQUID) magnetometer with a maximum field of 70 kOe. For the magnetic measurements, cold-pressed pellets of 5 mm in diameter and ~0.5 mm in thickness were made and the field was applied parallel to the flat surface of the pellet to reduce demagnetising effects.

3. Results and discussion

Fig. 1(a)–(e) shows XRD spectra of the powder mixtures that were milled for up to 4 h. It is evident that the intensity of diffraction peaks corresponding to $Fe_2(SO_4)_3$ and Na_2CO_3 decreased as the milling time increased. After 4 h of milling, the peaks corresponding to $Fe_2(SO_4)_3$ disappeared and the peaks associated with Na_2SO_4 appeared, indicating that the displacement reaction $Fe_2(SO_4)_3 + 3Na_2CO_3 \rightarrow Fe_2(CO_3)_3 + 3Na_2SO_4$ took place during milling. The peaks corresponding to $Fe_2(CO_3)_3$ were not detected after milling for 4 h, possibly due to the formation of amorphous phases.

The TG/DTA curves of the powder milled for 4 h is shown in Fig. 2. The weight loss that starts from ~630 K is associated with the thermal decomposition of $Fe_2(CO_3)_3$ [22]. The endothermic reaction that starts from ~850 K is associated with the eutectic melting of the NaCl and Na_2SO_4 mixture. Heat treatment above this temperature should be avoided because it will cause environmental problems associated with the decomposition of NaCl and Na_2SO_4 and also induce agglomeration of the particles [18]. Hence, in order to convert $Fe_2(CO_3)_3$ into Fe_2O_3, the as-milled powder was heat treated at 673 K for 1 h and then washed to remove Na_2SO_4 by-product and NaCl diluent. In Fig. 1(f), the XRD spectrum of the washed and dried powders consists of broad peaks which appears to correspond to maghemite (γ-Fe_2O_3 JCPDS #39-1346). However, due to the facts that the XRD pattern of maghemite (γ-Fe_2O_3) is nearly identical to that of magnetite (Fe_3O_4, JCPDS #19-0629) and that the diffraction peaks were highly broadened, it was not possible to identify the maghemite phase by XRD study only.

Fig. 3 shows TEM images of the sample after heat treatment and washing. It is evident that the sample consisted of nanoparticles with a low degree of agglomeration. The specific surface area of the

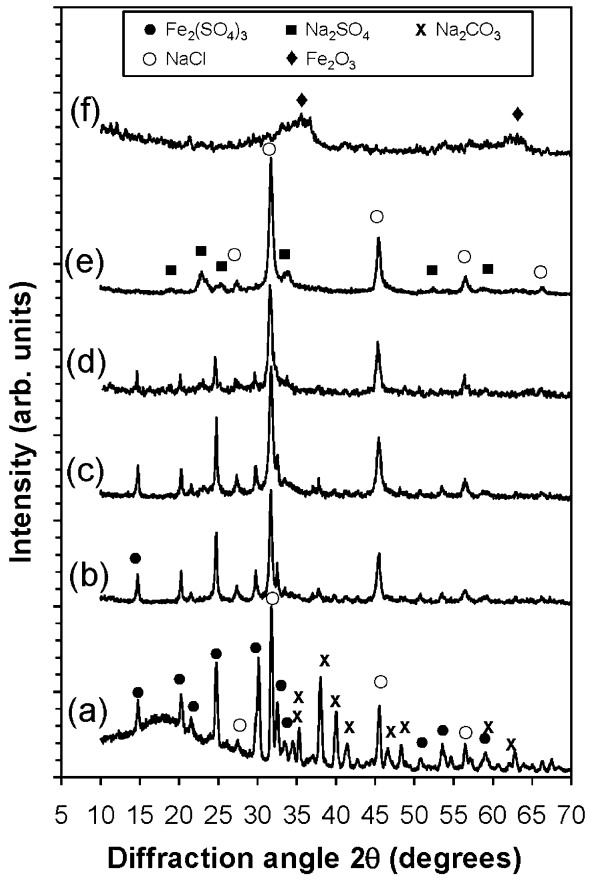

Fig. 1. XRD diffraction spectra of the as-milled powder mixtures of $Fe_2(SO_4)_3 + 3Na_2CO_3 + 4.3NaCl$ that were milled for (a) 0 h, (b) 0.5 h, (c) 1 h, (d) 2 h, (e) 4 h and (f) the spectrum of the powder that was milled for 4 h and subsequently heat treated at 400 °C and washed.

sample was 198 m^2/g, which corresponds to the spherical diameter of 6.2 nm using the following equation:

$$D = \frac{6000}{S\rho} \tag{3}$$

where D is the average particle diameter [nm], S is the specific surface area [m^2/g], and ρ is the density of the particle, 4.87 g/cm^3 [23]. The PCS volume-weighted particle size distribution in Fig. 4 showed a main peak at 6.3 nm and a very small peak at ~35 nm, indicative

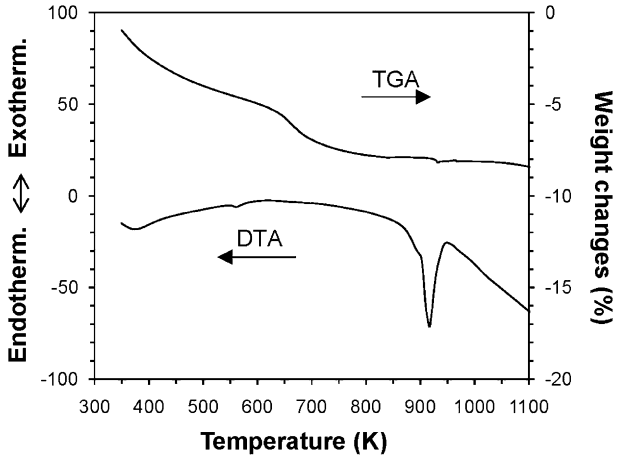

Fig. 2. TG/DTA curves of the powder mixture of $Fe_2(SO_4)_3 + 3Na_2CO_3 + 4.3NaCl$ that was milled for 4 h.

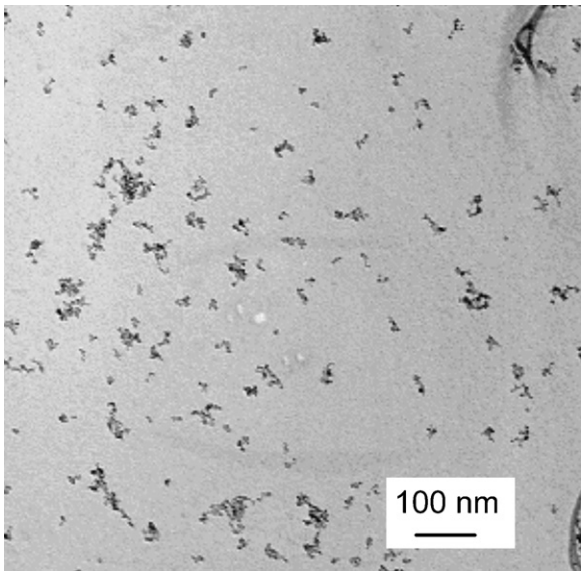

Fig. 3. TEM image of the Fe_2O_3 nanoparticles that was milled for 4 h and subsequently heat treated at 400 °C and washed.

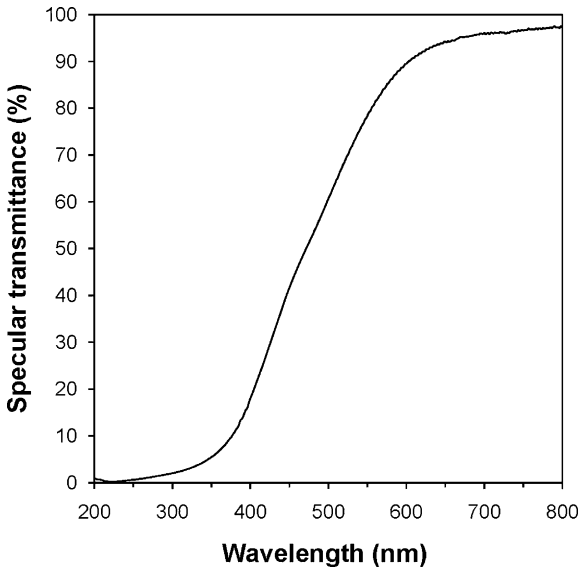

Fig. 5. UV–vis specular transmittance curves of the Fe_2O_3 nanoparticles dispersed in water.

of a significantly low degree of agglomeration. The standard deviation of the particle size distribution was 3.3 nm. The particle size estimated from the results of TEM, PCS and surface area analysis were in reasonable agreement with each other.

Fig. 5 shows UV–vis specular transmittance curve of the sample which shows significantly high transmittance, exceeding 90%, above 600 nm and low transmittance below 400 nm. The high transmittance in the visible light region is indicative of well-dispersed nanoparticles with an extremely low degree of agglomeration, which cause little light scattering as predicted by Mie scattering theory [24]. In fact, the particle suspension showed no visible turbidity at all, though strongly colored. The results demonstrate the promising applications of the nanoparticles as a transparent UV screening material [25].

As mentioned earlier, it was not possible to identify the maghemite (γ-Fe_2O_3) phase only by XRD study. However, it was possible to confirm the phase by UV–vis spectroscopy, as the bandgap energy of γ-Fe_2O_3 and Fe_3O_4 are largely different. In Fig. 5, the onset of light absorption appears to start from around 600 nm, which is close to the bandgap wavelength of bulk γ-Fe_2O_3, 610 nm [26]. Since Fe_3O_4 has a narrow bandgap of 0.14 eV and absorbs all the UV and visible light, the results of the UV–vis spectroscopy indicate that the sample that was heat-treated at 673 K consisted of mostly γ-Fe_2O_3.

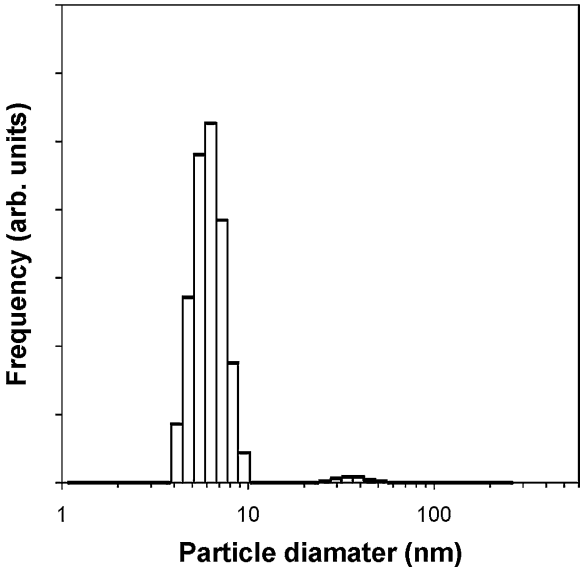

Fig. 4. Volume-weighted particle size distribution of the Fe_2O_3 nanoparticles.

Fig. 6(a) shows magnetic hysteresis loops measured at various temperatures; the same data are replotted in Fig. 6(b) with expanded axes to show details around the origin. All the measurements were made after cooling the sample from room temperature in the maximum field of 70 kOe. At 298 K, the hysteresis loop is characteristics of an S-shaped curve having no hysteresis, indicative of superparamagnetic nature, which is expected in these samples, having small particle sizes of 6–9 nm [14]. As the temperature is decreased from 298 to 100 K, the magnetisation increases significantly. Below 100 K, the overall shape of the hysteresis loop hardly changes but the coercivity (H_c) and remnant magnetisation (M_r) increase markedly below 50 K. At all temperatures, the magnetisation is far from saturation even in the maximum field of 70 kOe. Similar observations have been made in γ-Fe_2O_3 nanoparticles less than 10 nm in diameter produced by spray pyrolysis [27], mechanochemical processing via a NaOH route [20], and co-precipitation techniques [28]. The hysteresis loop measured at 5 K is displaced towards negative field (Fig. 6(b)), suggesting the presence of exchange anisotropy field.

In Fig. 6(c), the same hysteresis loops are replotted as a function of reduced field (H/T), where H is the magnetic field and T is the temperature. The data points for T = 298 and 100 K are superimposed on a single curve, indicating that the γ-Fe_2O_3 particles are indeed superparamagnetic at these temperatures. The magnetisation (M) of a system consisting of superparamagnetic particles is given by an equation involving the Langevin function [29]:

$$M = M_s \left(\coth \alpha - \frac{1}{\alpha} \right) = M_s \cdot L(\alpha) \quad (4)$$

where $L(\alpha)$ is the Langevin function, $\alpha = vM_s\rho H/k_BT$, M_s is the saturation magnetisation, v the volume of a particle, ρ the density of the material and k_B the Boltzmann constant. By fitting Eq. (4) to the data points for T = 298 and 100 K in Fig. 6(c), the M_s and v were determined to be 20.5 emu/g and 3.24×10^{-20} cm^3, respectively. For a spherical particle, the value of v corresponds to a diameter of 4.0 nm, which is considerably smaller than the particle size esti-

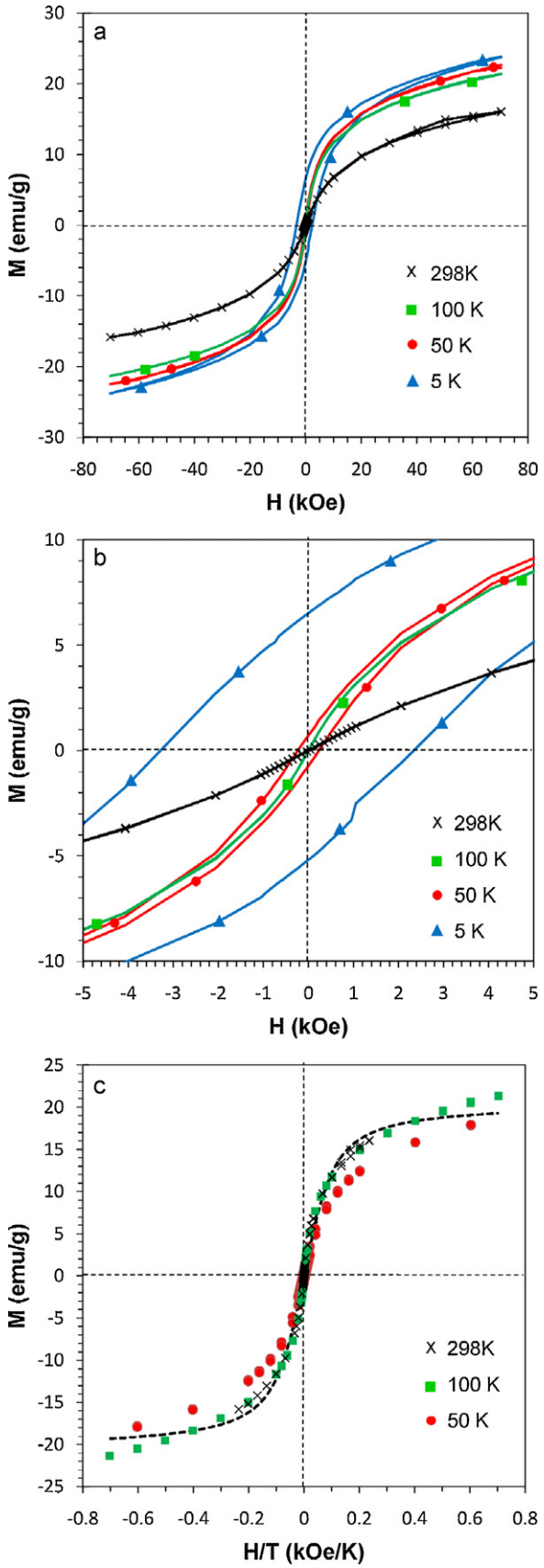

Fig. 6. (a) Hysteresis loops of γ-Fe_2O_3 nanoparticles, measured at various temperatures. (b) Enlargement of the hysteresis loops around the origin. (c) Hysteresis loops replotted as a function of reduced field (H/T). Dashed line: Fit of Eq. (4) to the data points for T = 298 and 100 K.

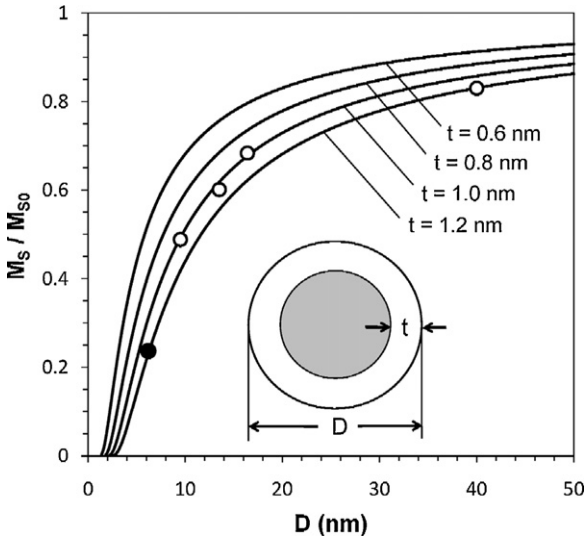

Fig. 7. Solid curves: particle-size (D) dependence of normalised saturation magnetisation (M_s/M_{s0}) for various values of shell thickness (t), calculated on the basis of Eq. (5); M_{s0} denotes the saturation magnetisation for bulk material. Filled circle: data point for γ-Fe_2O_3 sample heat treated at 400 °C (present work). Open circles: data points for $MnFe_2O_4$ nanoparticles [31]. Values of 87 and 80 emu/g were assumed as M_{s0} of γ-Fe_2O_3 and $MnFe_2O_4$, respectively. Inset: schematic picture of a particle, consisting of a ferrimagnetic core (shaded region) and a spin-glass shell.

mated from the BET and PCS measurements (6.2–6.3 nm). The value of M_s is also much smaller than that of bulk γ-Fe_2O_3, 87 emu/g [30].

These discrepancies in particle size and saturation magnetisation can be explained with a model in which it is assumed that each particle consists of a ferrimagnetic core having a collinear spin configuration and a magnetically disordered shell that makes little contribution to magnetisation [31]. According to this model, M_s will vary with particle size (D) as follows [31]:

$$\frac{M_S}{M_{S0}} = \frac{(D-2t)^3}{D^3} \quad (5)$$

where M_{s0} is the M_s for bulk material and t is the thickness of the shell. A series of theoretical M_s/M_{s0} vs D curves, corresponding to different values of t, are shown in Fig. 7. The data point (D, M_s/M_{s0}) = (6.2 nm, 20.5 emu/g) that was measured in the present study (filled circle) falls on the curve for t = 1.2 nm. This thickness is indeed close to half the difference between the particle size determined from the BET/PCS measurement (6.2–6.3 nm, which represents the size of a whole particle) and that from the magnetic measurement (4.0 nm, which represents the size of the ferrimagnetic core).

It is suggested that electrostatic disorder, i.e., the perturbation of crystal field, is primarily responsible for the surface spin disorder in spinel ferrites [31]. Since there are no ions outside the crystal, electrostatic potential near the particle surface is different from that deep inside the bulk, particularly in a crystal of primarily ionic character such as ferrites. This situation creates the perturbation of crystal field near the surface and affects the on-site Coulomb energy and the charge-transfer energy on ionic sites, resulting in the imbalance of the exchange coupling interaction and hence magnetic disorder [31].

For comparison, the data points (x, y) = (D, M_s/M_{s0}) for manganese ferrite nanoparticles, another crystal of primarily ionic nature [31], are also plotted in Fig. 7 (open circles). It is evident that the thickness of magnetically disordered shell in manganese ferrite nanoparticles is close to that of γ-Fe_2O_3 prepared in this study, indicating the universality of the model.

While the hysteresis loops for T = 298 and 100 K in Fig. 6(c) are reasonably well fitted by Eq. (4), the slope of the curve at high fields

appears to be greater than the theoretical prediction. This may be due to the contribution of the disordered spins in the shell to the magnetisation, neglected in the model. The disordered spins in the surface layer of spinal-ferrite nanoparticles can have a relatively large susceptibility in high fields [32].

Fig. 8 shows the temperature dependence of H_c, M_r and the exchange anisotropy field (H_a). It can be seen that both H_c and M_r become non-zero at 50 K and increase rapidly with decreasing temperature, while the H_a becomes non-zero at 20 K and increases with decreasing temperature. These features, also observed in nanoparticles of various spinel ferrites including γ-Fe_2O_3, are explained in terms of exchange coupling between the spins in the ferrimagnetic core and those in the magnetically disordered shell, assumed to be spin glass [14,28,31,33]: The spins in the shell become frozen below the spin-freezing temperature, making coherent rotation of the core spins more difficult, because of the core–shell exchange coupling; cooling in a field establishes a shell–spin configuration for which magnetisation of the core parallel to the field is energetically favourable, resulting in an exchange anisotropy field.

In Fig. 6(c), the data points for $T = 50$ K noticeably deviates from the common curve, suggesting that superparamagnetic blocking starts to occur at a temperature between 50 and 100 K. For non-interacting magnetic nanoparticles, the temperature dependence of H_c is described by the following equation [34]:

$$\frac{H_c(T)}{H_c(T=0)} = 1 - \left(\frac{T}{T_B}\right)^{1/2} \quad (6)$$

where T_B is the superparamagnetic blocking temperature. From Eq. (6), a linear relationship is expected between H_c and $T^{1/2}$. As shown in Fig. 9, the variation of H_c with $T^{1/2}$ is indeed well fitted by a straight line, and from its slope and intercept at $T^{1/2} = 0$, $H_c(T = 0)$ and T_B were calculated to be 4150 Oe and 56.6 K, respectively.

The superparamagnetic blocking temperature is related to the anisotropy constant (K) and the particle volume (v) via the following equation [14]:

$$T_B = \frac{KV}{25k_B} \quad (7)$$

Using the numerical values $T_B = 56.6$ K (derived immediately above) and $v = 3.24 \times 10^{-20}$ cm^3 (determined from the analysis of the hysteresis loops), K is estimated to be 6.03×10^6 erg/cm^3. This value is of the same order of magnitude as, but considerably greater than, the value derived by Sreeja and Joy from similar analysis, 1.32×10^6 erg/cm^3 [14]. The major reason for this discrepancy is

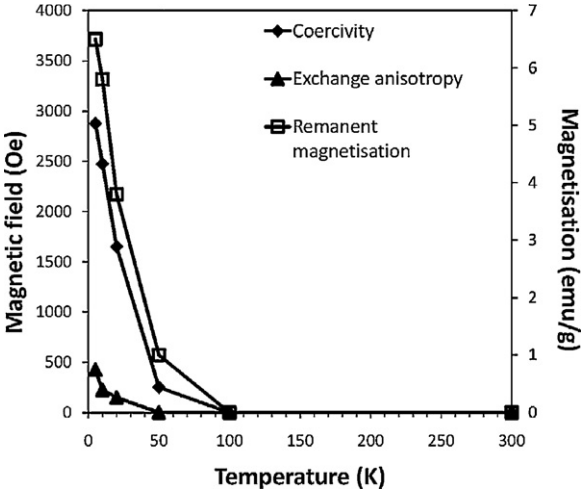

Fig. 8. Temperature dependence of coercivity, exchange anisotropy field and remanent magnetisation for the γ-Fe_2O_3 nanoparticles.

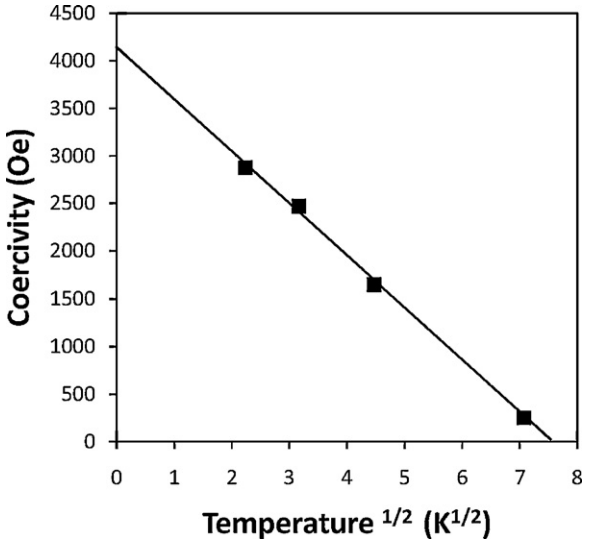

Fig. 9. Coercivity plot with respect to $T^{1/2}$ for the γ-Fe_2O_3 nanoparticles at 673 K. The fitting curve is displayed as a solid line.

that the latter value was derived using the volume of the whole particle including the magnetically disordered shell, resulting in an underestimate of K. In fact, the use of the whole particle volume corresponding to the particle size of 6.3 nm in our analysis leads to $K = 1.49 \times 10^6$ erg/cm^3.

The estimated K value is two orders of magnitude larger than the magnetocrystalline anisotropy constant for bulk γ-Fe_2O_3 (4.6×10^4 erg/cm^3) [30], suggesting that the exchange field originating from the magnetically disordered shell is almost entirely responsible for the high T_B as well as the high H_c at low temperature. The dominance of exchange anisotropy over magnetocrystalline anisotropy is likely to be the case with nanoparticles of all spinel ferrites except $CoFe_2O_4$ and its derivatives, which are known to have exceptionally large magnetocrystalline anisotropy ($K = 1.8$–3.4×10^6 erg/cm^3) [30] comparable to the K value derived above. It should be noted, however, that magnetocrystalline anisotropy, no matter how weak it may be, is necessary for the exchange field to be effective in preventing magnetisation reversal [32], without magnetocrystalline anisotropy the core and shell spins would be free to rotate coherently, keeping the relative spin configuration in the whole particle unchanged, and H_c would be zero.

4. Summary

In this study, magnetic properties of mechanochemically synthesised γ-Fe_2O_3 nanoparticles were investigated. By using a new reaction route, well-dispersed γ-Fe_2O_3 nanoparticles with a mean diameter of <10 nm and a narrow size distribution were synthesised, for the first time by mechanochemical processing. The γ-Fe_2O_3 particles showed a superparamagnetic nature. By fitting the hysteresis loop with the Langevin function, the saturation magnetisation and effective particle diameter were determined to be 20.5 emu/g and 4 nm, respectively. The effective magnetic diameter of the particle was smaller than the physical diameter of ~6 nm that was estimated by TEM, PCS and surface area analysis. The discrepancy was described with a model where each particle consists of a ferrimagnetic core having a collinear spin configuration and a magnetically disordered shell. The coercivity, M_r and the exchange anisotropy field increase rapidly with decreasing temperature below 50 K. The γ-Fe_2O_3 nanoparticles had the superparamagnetic blocking temperature of 56.6 K and the anisotropy constant of 6.0×10^6 erg/cm^3 which is two orders of magnitude

larger than the magnetocrystalline anisotropy constant for bulk γ-Fe_2O_3. These results were explained in terms of exchange coupling between the spins in the ferrimagnetic core and those in the magnetically disordered shell, assumed to be spin glass.

Acknowledgements

The authors acknowledge the Magnetics Laboratory of the School of Physics at the University of Western Australia for their assistance in conducting magnetic measurements. Electron microscopy study was carried out using facilities at the Center for Microscopy Characterisation and Analysis, the University of Western Australia, which is supported by University, State and Federal Government funding. The authors also thank Mr. Rongling He for his assistance in the aquisition of X-ray diffraction data.

References

[1] J.L. Dormann, D. Fiorani, Magnetic Properties of Fine Particles, North-Holland, New York, 1991.
[2] E. Katz, I. Willner, Chem. Commun. 45 (2005) 5641–5643.
[3] M. Zahn, J. Nanopartic. Res. 3 (2001) 73–78.
[4] Y.X.J. Wang, S.M. Hussain, G.P. Krestin, Eur. Radiol. 11 (2001) 2319–2331.
[5] S. Yan, D. Zhang, N. Gu, J. Zheng, A. Ding, Z. Wang, B. Xing, M. Ma, Y. Zhang, J. Nanosci. Nanotechnol. 5 (2005) 1185–1192.
[6] P. Gangopadhyay, S. Gallet, E. Franz, A. Persoons, T. Verbiest, IEEE Trans. Magn. 41 (2005) 4194–4196.
[7] A.R. Herdt, B.S. Kim, T.A. Taton, Bioconjug. Chem. 18 (2007) 183–189.
[8] R.F. Ziolo, E.P. Giannelis, B.A. Weinstein, M.P. O'Horo, B.N. Ganguly, V. Mehrotra, M.V. Russell, D.R. Huffman, Science 257 (1992) 219–223.
[9] H.K. Edwards, E. Evans, S. McCaldin, P. Blood, D.H. Gregory, M. Poliakoff, E. Lester, G.S. Walker, P.D. Brown, J. Phys. Conf. Ser. 26 (2006) 195–198.
[10] Z. Tianshu, P. Hing, Z. Ruifang, J. Mater. Sci. 35 (2000) 1419–1425.
[11] P. Zhang, Z.H. Yang, D.J. Wang, S.H. Kan, X.D. Chai, J.Z. Liu, T.J. Li, Synth. Met. 84 (1997) 165–166.
[12] C.J. Serna, M.P. Morales, in: E. Matijević, M. Borkovec (Eds.), Surface and Colloid Science, vol. 17, Kluwer Academic, New York, 2004.
[13] B. Hou, Y. Wu, L. Wu, Y. Shi, K. Zou, H. Gai, Mater. Lett. 60 (2006) 3188–3191.
[14] V. Sreeja, P.A. Joy, Mater. Res. Bull. 42 (2007) 1570–1576.
[15] S. Asuha, S. Zhao, H.Y. Wu, L. Song, O. Tegus, J. Alloys Compd. 472 (2009) L23–L25.
[16] T. Tsuzuki, P.G. McCormick, Mater. Sci. Forum 343–346 (2000) 383–388.
[17] P.G. McCormick, T. Tsuzuki, J.S. Robinson, J. Ding, Adv. Mater. 13 (2001) 1008–1010.
[18] T. Tsuzuki, P.G. McCormick, J. Am. Ceram. Soc. 84 (2001) 1453–1458.
[19] J. Ding, T. Tsuzuki, P.G. McCormick, Nanostruct. Mater. 8 (1997) 739–747.
[20] V. Kusigerski, M. Tadić, V. Spasojević, B. Antić, D. Marković, S. Bošković, B. Matović, Scr. Mater. 56 (2007) 883–886.
[21] I. Barin, Thermodynamical Data of Pure Substances, VCH, Weinheim, 1989.
[22] G. Zhang, K. Shen, D. Zhao, Y. Yuan, G. Wang, Mater. Lett. 62 (2008) 219–221.
[23] R.M. Cornell, U. Schwertmann, The Iron Oxides: Structure, Properties, Reactions, Occurrences and Uses, 2nd ed., Wiley-VCH, Weinheim, 2003.
[24] C.F. Bohren, D.R. Huffman, Absorption and Scattering of Light by Small Particles, Wiley, Toronto, 1998, pp. 130–157.
[25] F.J. Moloney, S. Collins, G.M. Murphy, Am. J. Clin. Dermatol. 3 (2002) 185–191.
[26] A. Cabot, A.F. Puntes, E. Shevchenko, Y. Yin, L. Balcells, M.A.M.S.M. Hughes, A.P. Alivisatos, J. Am. Chem. Soc. 129 (2007) 10358–10360.
[27] B. Martínez, A. Roig, A. Molins, T. González-Carreño, C.J.J. Serna, J. Appl. Phys. 83 (1998) 3256–3262.
[28] M.P. Morales, S. Veintemillas-Verdaguer, M.I. Montero, C.J. Serna, A. Roig, L.I. Casas, B. Martínez, F. Sandiumenge, Chem. Mater. 11 (1999) 3058–3064.
[29] S. Chikazumi, Physics of Magnetism, John Wiley & Sons, New York, 1964.
[30] V.A.M. Brabers, in: K.H.J. Buschow (Ed.), Handbook of Magnetic Materials, vol. 8, Elsevier, Amsterdam, 1995.
[31] M. Muroi, R. Street, P.G. McCormick, J. Amighian, Phys. Rev. B: Condens. Matter 63 (2001) 184414.
[32] M. Muroi, P.G. McCormick, R. Street, Rev. Adv. Mater. Sci. 5 (2003) 76–81.
[33] E. Tronca, D. Fioranib, M. Nogüesc, A.M. Testab, F. Lucarid, F.D.O.J.M. Grenechee, W. Wernsdorferf, N. Galvezg, C. Chaneaca, D. Maillyh, J.P. Joliveta, J. Magn. Magn. Mater. 262 (2003) 6–14.
[34] B.D. Cullity, Introduction to Magnetic Materials, Addison-Wesley, Reading, 1972, pp. 410–418.